**Structural Monitoring and Maintenance**, *Vol. 8, No. 4 (2021) 345-360*
https://doi.org/10.12989/smm.2021.8.4.345


# Buckling failure of cylindrical ring structures subjected to coupled hydrostatic and hydrodynamic pressures

Liu Ping [1a], Yang Xin Feng [1b] and Chayut Ngamkhanong*[2]

[1] *Department of Civil Engineering and Architecture, Jiangsu University of Science and Technology, Zhenjiang 215003, China*
[2] *Department of Civil Engineering, Faculty of Engineering, Chulalongkorn University, Bangkok 10330, Thailand*

(*Received April 19, 2021, Revised October 4, 2021, Accepted October 8, 2021*)

**Abstract.** This paper presents an analytical approach to calculate the buckling load of the cylindrical ring structures subjected to both hydrostatic and hydrodynamic pressures. Based on the conservative law of energy and Timoshenko beam theory, a theoretical formula, which can be used to evaluate the critical pressure of buckling, is first derived for the simplified cylindrical ring structures. It is assumed that the hydrodynamic pressure can be treated as an equivalent hydrostatic pressure as a cosine function along the perimeter while the thickness ratio is limited to 0.2. Note that this paper limits the deformed shape of the cylindrical ring structures to an elliptical shape. The proposed analytical solutions are then compared with the numerical simulations. The critical pressure is evaluated in this study considering two possible failure modes: ultimate failure and buckling failure. The results show that the proposed analytical solutions can correctly predict the critical pressure for both failure modes. However, it is not recommended to be used when the hydrostatic pressure is low or medium (less than 80% of the critical pressure) as the analytical solutions underestimate the critical pressure especially when the ultimate failure mode occurs. This implies that the proposed solutions can still be used properly when the subsea vehicles are located in the deep parts of the ocean where the hydrostatic pressure is high. The finding will further help improve the geometric design of subsea vehicles against both hydrostatic and hydrodynamic pressures to enhance its strength and stability when it moves underwater. It will also help to control the speed of the subsea vehicles especially they move close to the sea bottom to prevent a catastrophic failure.

**Keywords:** buckling; critical load; cylindrical structure; failure mode; plastic yielding; submarine structure

## 1. Introduction

At present, underwater vehicles are increasingly needed for the investigation and exploration of ocean graphic resources, and subsea operations at ever greater depths (Durban and Libai 1972, Tvergaard 1983, Cho *et al*. 2019, Li *et al*. 2019a, b). This can induce a very high pressure acting on the vehicles especially when subsea vehicles are travelling in a very deep sea. In general, the

*Corresponding author, Ph.D., E-mail: chayut.ng@chula.ac.th
[a] Associate Professor, Ph.D., E-mail: liupinghaiyan@163.com
[b] M.Eng., E-mail: yangxinfeng3460@163.com

**Copyright © 2021 Techno-Press, Ltd.**
http://www.techno-press.org/?journal=smm&subpage=7 ISSN: 2288-6605 (Print), 2288-6613 (Online)

bearing capacity of high hydrostatic pressure around subsea vehicles is mainly provided by the cylindrical shell (Stuart *et al*. 1968, Hongwei *et al*. 1999, Qu *et al*. 2019, Rizzetto *et al*. 2019). Therefore, the cylindrical hull plays a key role in deep submersibles in encountering an external pressure. It does not only provide the capability for resisting the external hydrostatic pressure, but also the ability for bearing the hydrodynamic pressure induced by fluid around the cylindrical shell. In real application, due to a larger workspace and high hydrostatic pressure in the sea, the shape of the submarine is usually made as a cylindrical shell in order to bear a high hydrostatic pressure underwater. It is noted that deep submersible vehicles have a composite cylindrical pressure hull which can effectively bear high external hydrostatic pressure (Zou and Foster 1995, Ganesan and Pradeep 2005). Many previous studies have conducted the studies on buckling behaviour of cylindrical shells subjected to hydrostatic pressure only while, in fact, the pressure is usually added up by the hydrodynamic pressure when structures move or are hit by a strong wave (Timmins and O'Young 2009, McClain and Barry 2010, Faridmehr *et al*. 2019) while the previous analytical approaches do not include such extra loads into their formulae. The first analytical result was derived using small deflection theory (Pang *et al*. 2019). The study provided the formula for the stability of a thin free-standing circular cylindrical ring under hydrostatic pressure as shown in Eq. (1).

$$P_{cr} = 3EI/R^3 \tag{1}$$

Where $E$ is the modulus of elasticity; $I$ is the inertia moment of the cross section, $R$ is the radius of the mid-surface of the cylindrical structure and $P_{cr}$ is the critical buckling pressure. Furthermore, considering the effect of Poisson's ratio, Eq. (2) is presented using the principle of minimum potential energy (Sun *et al*. 2012, Pi and Bradford 2013).

$$P_{cr} = \frac{2E}{1-v^2}\left(\frac{t}{D}\right) \tag{2}$$

Where, $D$, $t$, $v$ are the diameter, thickness and Poisson's ratio of the cylindrical shell, respectively. Note that Eq. (2) can be obtained by replacing $E$ as and substituting $I = t^3/12$ into Eq. (1). It is noted that these equations represent linear stability phenomena for general structures under static load only. Detailed studies into the structural behaviours of the cylindrical ring under realistic loads are still needed.

Recently, many researchers have conducted studies on the structural stability of subsea vehicle. Pi and Bradford (2013) studied the in-plane stability of preload shallow arches acting upon dynamic snap-through accounting for rotational end restraints. They considered a sudden-applied load and discussed the dynamic snap-through owing to excessive oscillations reaching its unstable branch. A series of studies on a semi-analytical method for free vibration analysis of both cylindrical and spherical shells was conducted (Li *et al*. 2019a, b). They used the approach of Rayleigh-Ritz to obtain conclusions on the free vibration behaviours of cylindrical and spherical shells. A detailed asymptotic analysis of the point indentation of an unpressurized spherical elastic shell was studied (Gomez *et al*. 2016). This implied that the shell can be deformed by 'mirror buckling' - a portion of the shell inverts to become a spherical cap with equal but opposite curvature to the undeformed shell. A series of experiments on the dynamic plastic buckling of circular cylindrical shells under axial impact load was carried out (Wang *et al*. 2014, Ma *et al*. 2016). They found two different kinds of non-asymmetric buckling shapes: oval-shaped and triangle shaped. However, they did not consider the various loads acting on the structure. The

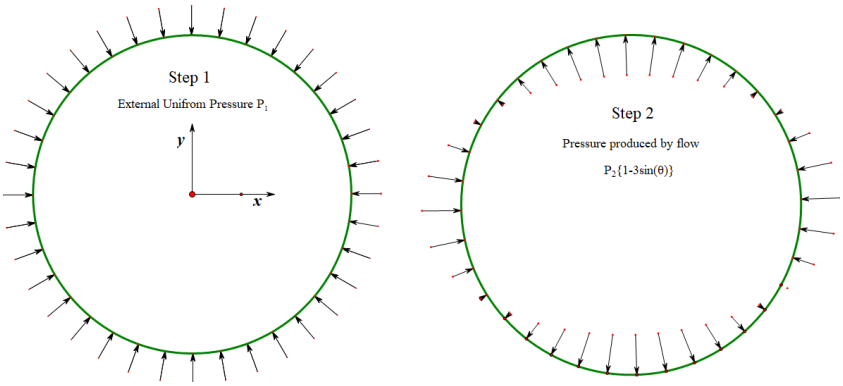


Fig. 1 The distribution patterns of hydrostatic and hydrodynamic pressure

nonlinear elastic stability of arches via the principle of virtual work considering geometrical nonlinearity was studied, but the load was assumed to be in a constant direction (Hu *et al*. 2018, Hu and Huang 2019). A report on the buckling of thin-walled circular cylinders under axial compression and bending with the financial support of NASA was published (Stuart *et al*. 1968). They completed a series of tests on both electroplated copper and Mylar cylinders under combined axial compression and bending (Maier *et al*. 2017, Constable *et al*. 2018, Enrichetti *et al*. 2018). They obtained much higher buckling stress values than those reported before. Recently, Hernandez, Naranjo and Vellojin (Hernandez *et al*. 2020) found a new constitutive equation in integral form.

$$P = P_1 + P_2(1 - 4\sin(\theta)^2) \tag{3}$$

It is notably that the buckling phenomena of the circular cylindrical shell subjected to both hydrostatic and hydrodynamic pressure loads, which usually occur in the working state (Timmins and O'Young 2009, McClain and Barry 2010, Berkenpas *et al*. 2018), have never been fully investigated in the past. In reality, the hydrodynamic pressure is largely produced when the vehicle is moving underwater. This can create different structural behaviour and failure mechanism of vehicle from the external hydrostatic pressure only. The load distribution patterns of the hydrostatic and hydrodynamic pressures are presented in Fig. 1 and the combination of both pressures is presented in Eq. (3). It is important to note that there are many differences between the buckling phenomena caused by hydrostatic load only and combined pressures (Franzoni *et al*. 2019a, b, Lu *et al*. 2019). This paper is the first to discuss this problem and provides a new theoretical approach to evaluate the buckling capacity of the circular cylindrical shell subjected to both hydrostatic and hydrodynamic pressures. The outcome will help facilitate the primary geometric design of the subsea vehicle in order to prevent buckling instability phenomena under hydrostatic and hydrodynamic pressures.

## 2. Analytical solution

### *2.1 Deformed shape*

Generally, the thickness ratio (thickness/radius) is about 5-20% for subsea vehicle. This leads to the ellipse deformation shape, as shown in Fig. 2 (Narayana *et al*. 2013, Franzoni *et al*. 2019a, b).

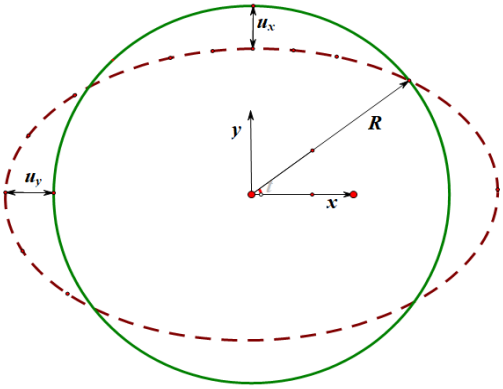


Fig. 2 Deformed shape of circular ring

The original circular radius is noted as $R$. The deformation parameters are expressed as $u_x$, $u_y$ that are related to the deformation of the semi-major axis and semi-minor axis, respectively. The length of semi-major and semi-minor axis of $a, b$ after buckling are defined as shown in Eq. (4) below.

$$a = R + u_x, \qquad b = R - u_y, \tag{4}$$

Obviously, the perimeter has a very small change after deformation. Therefore, the relationship of $u_x$, $u_y$ can be limited by Eq. (5), where the eccentricity of $e$ is defined as $e^2 = 1 - b^2/a^2$.

$$1 = \left(1 + \frac{u_x}{R}\right)\left(1 - \frac{1}{4}e^2\right) \quad \Rightarrow \quad u_x = u_y = u \tag{5}$$

According to Eq. (5), it can be seen that the increment of semi-major axis is equal to the decrement of the semi-minor axis. Hence, both $u_x$, $u_y$ can be equally denoted as $u$.

It is well known that the elliptic integral of the second kind can be written in the asymptotic expressions as shown in Eq. (6).

$$E(e,\theta) = \theta - \frac{1}{2}e^2 \int_0^\theta sin^2(\varphi)d\varphi - \frac{1}{8}e^4 \int_0^\theta sin^4(\varphi)d\varphi \cdots \tag{6}$$

Further, the internal energy is calculated from the stretching and bending strain. The stretching strain of the middle surface of the shell is shown in Eq. (7). Also, it can be seen that the stretching strain is proportional to the square of $u$.

$$\varepsilon_m = \frac{u}{r} + \frac{\partial u}{\partial \theta} = \frac{2u^2}{R^2}, \qquad \delta\varepsilon_m = \frac{4u}{R^2}\delta u \tag{7}$$

As for the changes of curvature, it can be expressed as shown in Eq. (8) (Fujita and Nosaka 2002, Okubo *et al*. 2003), where $\rho'$ is the radius of the shell after deformation. It is convenient to get $\frac{1}{\rho'} = \frac{1}{R} + \frac{3u}{R^2}(2\cos(\theta)^2 - 1)$ when the 2nd term is neglected.

$$\kappa = \frac{1}{\rho'} - \frac{1}{R} \tag{8}$$

Taking the analysis of deformation above into account, we can deduce the Eq. (9) from Eq. (8). In addition, we can obtain the expression of curvature changes and the virtual work from curvature denoted with the parameter $u$.

$$\kappa = \frac{3u}{R^2}\cos(2\theta), \qquad \delta\kappa = \frac{3\cos(2\theta)}{R^2}\delta u \tag{9}$$

### *2.2 Principle of virtual work*

Considering the energy from stretching and bending strain, we can establish the control equation illustrated in Eq. (10) on the basis of principle of virtual work.

$$\oint EA\varepsilon_m \delta\varepsilon_m \cdot ds + \oint EI\kappa\delta\kappa \cdot ds = \oint pds \cdot \delta u \tag{10}$$

Considering the characteristic of hydrostatic pressure deduced by the deep water, we can see that the pressure is always in the normal direction of surface. This means that the direction can be changed as the deformation occurs. Therefore, $p \cdot ds = p(R + 3u\cos(2\theta))d\theta$ and we can simplify Eq. (10) by substituting Eqs. (7) and (9).

$$\begin{aligned} &\oint EA\frac{2u^2}{R^2}\cdot\frac{4u}{R^2}\delta u ds + \oint EI\frac{3u}{R^2}\cos(2\theta)\frac{3\cos(2\theta)}{R^2}\delta u ds \\ &= \oint P(R + 3u\cos(2\theta))\cos(2\theta)\,\delta u d\theta \end{aligned} \tag{11}$$

Owing to $\delta u$ being the arbitrary displacement, we can simplify Eq. (12) as follows

$$\oint \left(\frac{\pi EA}{8}\frac{u^3}{R^3} + \frac{9EIu}{R^3}\cos(2\theta)^2\right)\cdot \delta u d\theta = 3P\pi u \cdot \delta u \tag{12}$$

Considering $u$ is extremely small compared to $R$, it is reasonable to neglect the 1st term of $u^3$, and we can simplify it as follows

$$\frac{9EI\pi u}{R^3} = 3P\pi u \qquad \Longrightarrow \qquad P_{cr} = \frac{3EI}{R^3} \tag{13}$$

According to the Eqs. (12) and (13), we can see that in the case of considering both hydrostatic $P_1$ and hydrodynamic $P_2$ pressure, only the term with pressure is different. Therefore, we can simplify Eq. (12) as Eq. (3). Considering the arbitrary $\delta u$, it can be represented as follows

$$(P_1 - P_2) + \frac{2}{3}P_2\frac{R}{u} = P_{cr} \tag{14}$$

Where $P_{cr}$ is the critical pressure in the case of combined pressure. From Eq. (14), the displacement $u$ is determined by the hydrostatic and hydrodynamic pressures. However, the

displacement is limited to a certain small range according to the ultimate strength of the material. It is assumed that the cylindrical shell buckles when any point is in a plastic state, so the maximum displacement is limited by Eq. (15)

$$\frac{3u}{R^2}\frac{t}{2} = \varepsilon_s \qquad \Longrightarrow \qquad u_m = \frac{2}{3}\frac{R^2}{t}\varepsilon_s \tag{15}$$

Where $\varepsilon_s$ is the yielding strain of material. When the structure is in the plastic state, let denoted $p_1 = P_1/P_{cr}$, $p_2 = P_2/P_{cr}$ and $u = t/R$, Eq. (14) can be simplified as

$$p_1 + p_2 \cdot \left(\frac{\mu}{\varepsilon_s} - 1\right) = 1 \tag{16}$$

After substituting $\alpha = \frac{\mu}{\varepsilon_s} - 1$ in Eq. (16), Eq. (17) can be obtained.

$$p_1 + \alpha \cdot p_2 = 1 \tag{17}$$

Hydrodynamic pressure is a very different type of pressure compared to hydrostatic pressure. However, from Eqs. (16) and (17), it can be seen that the hydrodynamic pressure is an equivalent hydrostatic pressure on the basis of the transformation rules. In addition, if the cylindrical structure does not deform as an ellipse, it is reasonable to create a hypothesis that the structure will deform as a harmonic function as described in Eq. (18)

$$r = R + u \cdot \cos(2\theta) \tag{18}$$

Firstly, we can obtain changes in the curvature shown in Eq. (19). We can see that the curvature in this deformation is the same as Eq. (9). This means that the identical critical pressure with the deformation can be obtained as described earlier.

$$\kappa = \frac{1}{\rho'} - \frac{1}{R} = \kappa = \frac{3u}{R^2}\cos(2\theta) \tag{19}$$

In the previous section, it is assumed that the structures buckle before entering a plastic state. However, the failure mode can be different as the structure may reach the ultimate strength state before buckling. In such case, Eq. (17) is also applicable, but the critical pressure should be adapted as follows where $\sigma_s$ is the critical stress.

$$P_{cr} = \sigma_s \cdot \mu \tag{20}$$

## 3. Finite Element Method (FEM)

### *3.1 Model description*

To verify the theoretical solution, numerical simulations are carried out using Finite Element Method (FEM) with ANSYS 2020. The radius of the cylindrical shell is set as 1.0 meter and the section profile is 1.0 metre wide, and 0.1 metre height. In light of mechanics, such a cylindrical shell can be considered as a 2-D problem. The front view with a distributed pressure is shown in

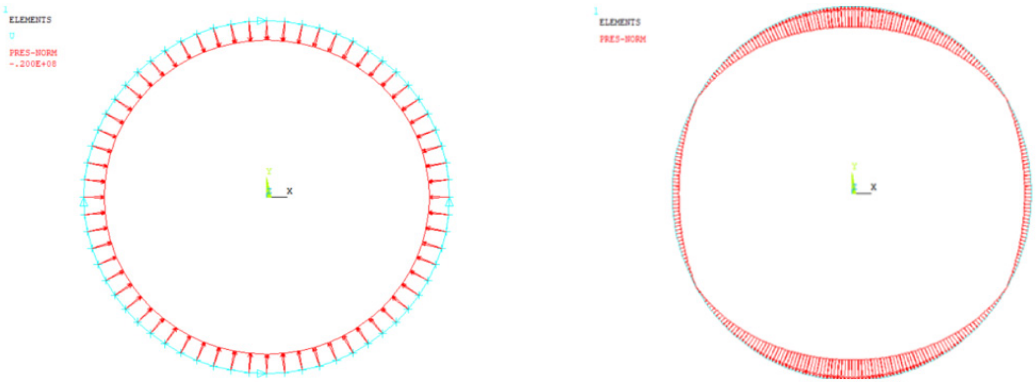

(a) Hydrostatic pressure (Load step 1) (b) Hydrodynamic pressure (Load step 2)

Fig. 3 Pressure distribution on a circular ring

Table 1 The comparison of the elastic energy (kJ) with different mesh size (m)

| Mesh size | 0.2 | 0.15 | 0.1 | 0.08 | 0.05 | 0.03 | 0.02 | 0.01 |
|---|---|---|---|---|---|---|---|---|
| Elastic energy | 14.76 | 14.81 | 14.89 | 14.90 | 14.92 | 14.93 | 14.93 | 14.93 |

Fig. 3. Furthermore, the pressure is set as a parameter in different cases of simulation. It should be noted that the directional pressure changes after deformation.

In this study, steel is considered as a cylindrical shell as it provides better performance underwater than other materials (Zou *et al*. 2018, Werner 2019). The elastic modulus is set as 210 GPa, the yield stress $\sigma_s$ is 210 MPa and the yield strain $\varepsilon_s$ is 0.1%. Therefore, in this case, the critical pressure would be $P_{cr} = 21\ MPa$.

$$M_u = \frac{\sigma_s t^2}{4} = 525\ \text{kN.m}, \qquad P_{cr}^1 = 52.5\ \text{MPa}, \qquad P_{cr}^2 = \sigma_s \mu = 21\ \text{MPa} \tag{21}$$

The circular ring model is made of the beam element (188 elements based on Timoshenko beam theory). According to the real condition in the application, two load steps are set including the first load step being the hydrostatic pressure $p_1$ and the second load step being the hydrodynamic pressure $p_2$ whose distribution is deduced by the potential flow theory, which is illustrated in Fig. 3. Both the rightmost and leftmost nodes are constrained in Y-direction. In addition, the highest and lowest nodes are constrained in X-direction. A nonlinear effect is considered and 10-time steps is set in the first load step, and 100 time steps are set in the second load step. Mesh convergence analyses has been conducted in order to optimise the proper mesh size. Table 1 illustrates the elastic energy with different mesh sizes which is also plotted in Fig. 4. It can be seen from the plot that the total elastic energy has no change when the mesh size is smaller than 0.03 m. Hence, the size of element is set as 0.02 m to ensure its accuracy and reduce time consuming.

### *3.2 Model validation*

The deformed shape of the cylindrical shell is carried out under the critical pressure. Fig. 5

shows the radial displacement (in the cylindrical coordinate, X-directional displacement means the radial displacement). It can be seen that all the displacements of the rightmost, leftmost, highest and lowest points have the identical values of 0.846 mm, which concurs with the analytical solution.

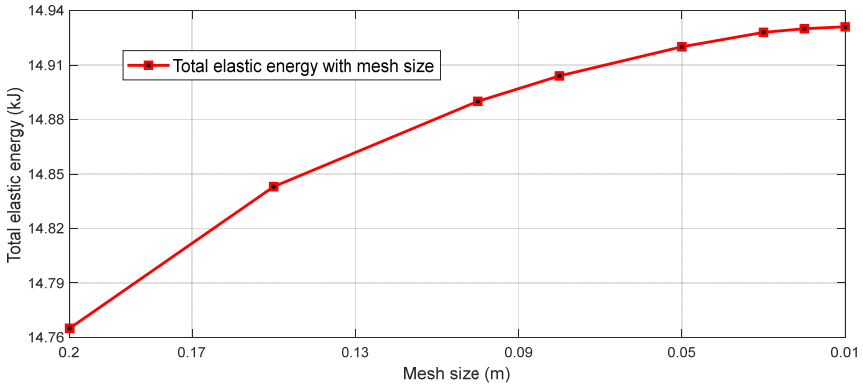


Fig. 4 Mesh convergence analysis

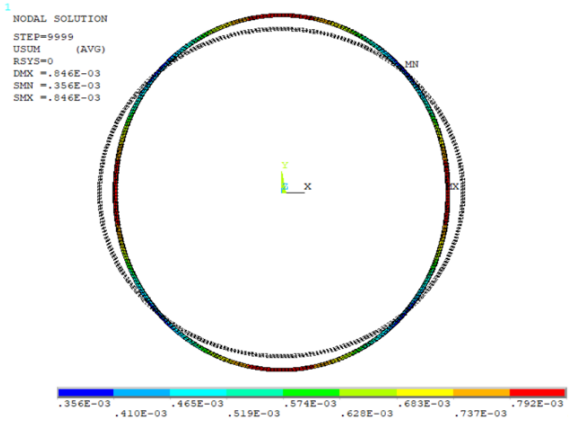


Fig. 5 Radial displacement of deformed circular ring (scale = 3.0)

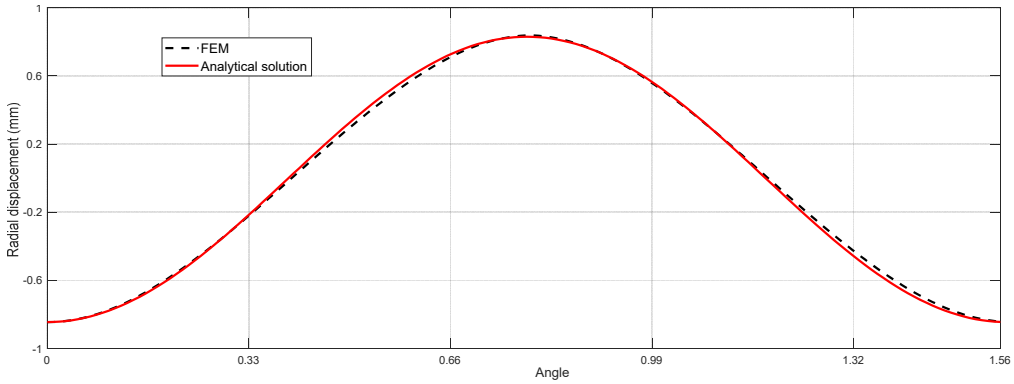


Fig. 6 Radial displacement vs the circumference angle of half ring

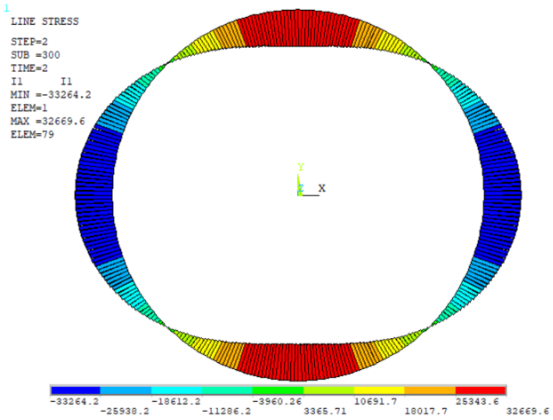


Fig. 7 The contour of moment

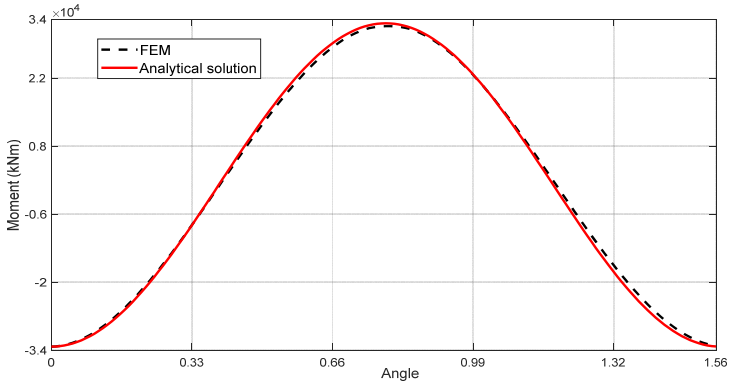


Fig. 8 Moment vs circumferential angle of half ring

Fig. 6 shows the results of the radial displacement along the circumference degree. The result of half part is presented as the cylindrical structure buckles a symmetrical shape. The results of FEM and analytical solution are compared. It is found that the FEM results match well with the analytical solution as shown in Fig. 6.

Fig. 7 presents the contour plot of the moment across the circumference of the cylindrical structure while Fig. 8 is the plot of moment and the circumferential angle relationship. It can be seen that the numerical result agrees well with the analytical results. Based on the radial displacement and moment in the cylindrical shell derived from numerical simulation. It can be concluded that the verified FEM model can be sufficiently used further.

## 4. Results

### *4.1 Time history analysis*

Fig. 9 presents the displacement time history of the highest and leftmost nodes under the critical pressure of 21 MPa calculated using Eq. (21). It should be pointed out that the plot starts from $t$ = 1.0 which is the end time step of the hydrostatic pressure. This shows that the hydrostatic

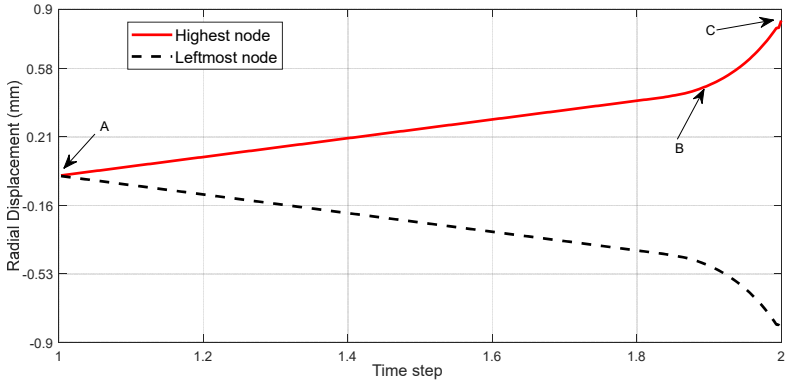


Fig. 9 Radial displacement at the highest and leftmost points under the calculated critical pressure

pressure produces little displacement. After applying hydrodynamic pressure, it can be seen in this plot that the displacement response has turning points at point B ends at point where the pressure of 21 MPa is applied. At point B, the structure reaches the yield state at the pressure of 19.9 MPa at point B. Between B and C, the displacement increases significantly due to the change from elastic stage to plastic stage. As described above, in this case, there is no bifurcation. It should be noted that there is no data obtained after point C as the simulation stops at this point. Between stages. It is important to note that the critical pressure applied is the estimation made by analytical solution. It is unclear whether the pressure is a buckling pressure as the postbuckling stage cannot be seen clearly. Hence, it is important to enhance to simulation by increasing the pressure to correctly estimate the buckling pressure.

As described above, it is difficult to obtain the actual critical load from Fig. 9. This is because the structure may still bear some load after the last time step. Thus, the simulation with larger load is conducted to accurately obtain the critical load.

Fig. 10 depicts the time history of displacement on the highest and leftmost points under the hydrodynamic pressure. There are also two turning points, B and C. However, the displacement drops dramatically, which means the analysis could not go further for larger displacement due to the buckling. Therefore, the corresponding load is remarked as the critical load.

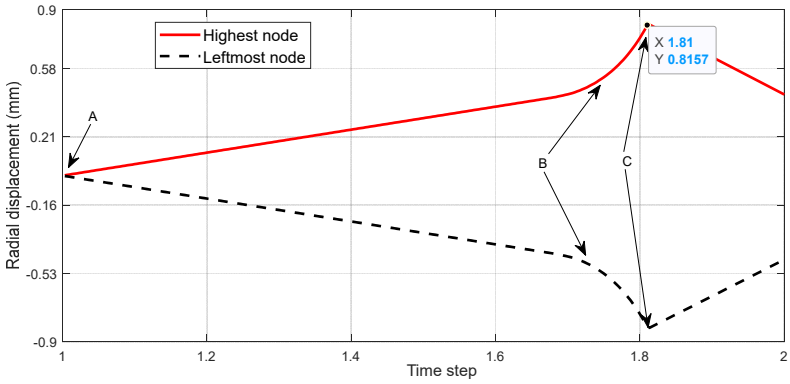


Fig. 10 Radial displacement at the highest and leftmost nodes including post-buckling stage

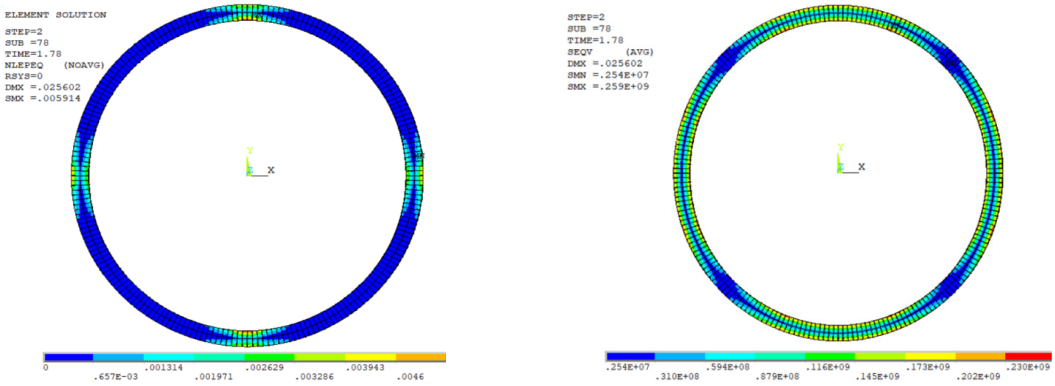


Fig. 11 The contour plot of plastic strain and stress under the pressure of 21 MPa

Fig. 11 shows the contour plot of the plastic strain and stress at time step of 1.81 under the critical pressure of 21 MPa. There are 4 regions where plastic strain appears. Two regions lay in the outer area close to the highest and lowest points of the circular ring while the other two lay in the inner area close to the rightmost and leftmost points of the ring. These characteristics are also revealed in the contour plot of stress. It shows the regions, where plastic strain doesn't appear, are still in an elastic state. This means that the areas, which lay on the perpendicular line, do not enter a plastic state simultaneously.

### *4.2 Parametric study*

#### *4.2.1 Case 1: Ultimate failure*

Using the methods shown above, we have carried out a number of numerical simulations considering different $p_1$, $p_2$ with the thickness of 0.1, 0.2, respectively. These results are shown in Table 2. It is shown that the summation of functions of hydrostatic and hydrodynamic pressures is greater than 1 meaning that the failure mode is the ultimate failure.

Fig. 13 shows the results of hydrodynamic pressure $p_2$ with the hydrostatic pressure $p_1$. The black solid line is derived using the analytical solution of Eq. (17). The black solid circle is the FEM result with $\mu$ = 0.1 and $\mu$ = 0.2. It can be concluded that the results of FEM agree very

Table 2 Results of $p_1$ with different $p_2$ for Case 1

| Case | $R$ (m) | $t$ (m) | $p_1$ | $\alpha \cdot p_2$ | $p_1 + \alpha \cdot p_2$ |
|---|---|---|---|---|---|
| 1 | 1 | 0.1 | 0.67 | 0.69 | 1.36 |
| 2 | | | 0.76 | 0.45 | 1.21 |
| 3 | | | 0.86 | 0.24 | 1.10 |
| 4 | | | 0.90 | 0.17 | 1.07 |
| 5 | | | 0.95 | 0.08 | 1.03 |
| 6 | | 0.2 | 0.61 | 0.62 | 1.23 |
| 7 | | | 0.75 | 0.71 | 0.94 |
| 8 | | | 0.83 | 0.26 | 1.09 |
| 9 | | | 0.95 | 0.08 | 1.03 |

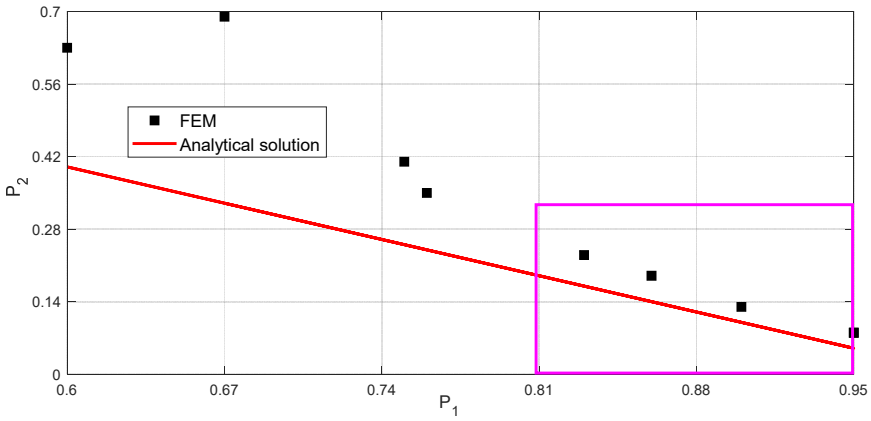


Fig. 12 $p_2$ against $p_1$ for Case 1

well with the prediction when the $p_1$ is close to the critical load. However, when the hydrostatic pressure $p_1$ is small, especially smaller than 0.8, there are 30% more errors between the analytical solution and FEM results. This shows that the analytical solution underestimates the critical hydrodynamic pressure.

#### *4.2.2 Case 2: Buckling failure*

In this case, the radius is increased from 1 m to 2 m while the thickness is similar to the previous section in order to reduce the thickness ratio and study another failure condition. Due to the change in geometry, the parameters $\mu$ of 0.05 and 0.1 are considered. The results of the nominal pressures $p_1$ and $p_2$ are listed in Table 3. It should be noted from Eq. (22) that the critical pressure of buckling is less than the ultimate strength. Therefore, the buckling critical pressure $P_{cr}^1$ is expected to be the critical load in this condition.

$$P_{cr}^1 = 6.56 \text{ MPa}, \qquad P_{cr}^2 = \sigma_s \mu = 10.5 \text{ MPa} \tag{22}$$

Fig. 14 shows the results of hydrodynamic pressure $p_2$ against the hydrostatic pressure $p_1$ in Case 2. The result shows that the FEM results agree very well with the theoretical prediction of

Table 3 Results of $p_1$ with different $p_2$ for Case 2

| Case | $R$ (m) | $t$ (m) | $p_1$ | $\alpha \cdot p_2$ | $p_1 + \alpha \cdot p_2$ |
|---|---|---|---|---|---|
| 1 | 2 | 0.1 | 0.04 | 0.90 | 0.94 |
| 2 | | | 0.23 | 0.70 | 0.93 |
| 3 | | | 0.51 | 0.45 | 0.96 |
| 4 | | | 0.75 | 0.20 | 0.95 |
| 5 | | | 0.90 | 0.10 | 1.0 |
| 6 | | 0.2 | 0.024 | 0.90 | 0.924 |
| 7 | | | 0.241 | 0.70 | 0.941 |
| 8 | | | 0.443 | 0.45 | 0.993 |
| 9 | | | 0.672 | 0.15 | 0.822 |

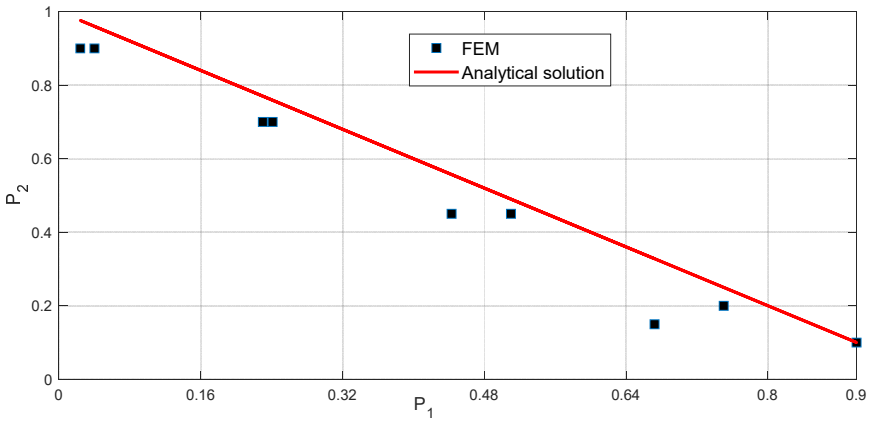


Fig. 13 $p_2$ against $p_1$ for Case 2

this paper. In comparison to the results in case 1, the same characteristic is presented here as Case 1.

As a result, it can be concluded that there are two types of failure of the circular cylindrical shell under both external hydrostatic pressure and hydrodynamic pressure. The first mode of failure is when the pressure exceeds the ultimate strength of material. In this case, the critical pressure $P_{cr}$ should be calculated by Eq. (20). The second mode of the failure is the buckling of the structure. In this case, the critical pressure $P_{cr}$ should be calculated by Eq. (13).

On the condition of hydrostatic pressure $p_1$ being more than 0.8, the hydrostatic pressure $p_1$ and hydrodynamic pressure $p_2$, the results from FEM agree with Eq. (17) very well for both failure modes especially when the hydrostatic pressure is larger than 0.8. However, if hydrostatic pressure is smaller than 0.8, the assumption of ellipse deformation is not accurate especially when the ultimate failure mode occurs as shown in Case 1. Therefore, the error between theoretical solution and the FEM value will increase as there is a decrease in $p_1$. Nevertheless, in the actual application, the investigation of subsea vehicle, submarine, etc., are usually under the condition when $p_1$ = 0.8, 0.9 or even more. Thus, this study confirms that Eq. (17) can be used to estimate the $p_2$ which is linked to the velocity of the subsea vehicle.

## 5. Conclusions

This paper investigates the in-plane nonlinear elastic stability of the circular ring structures subjected to both hydrostatic and hydrodynamic pressure. Based on the principle of energy, the relationship between the hydrostatic and hydrodynamic pressure in the buckling state is concluded in this study. A series of numerical simulations are conducted to verify the theoretical solutions considering the two possible failure modes: ultimate strength and buckling failure when such circular ring structure bears uniform pressure only. It is largely influenced by the elastic modulus and the thickness ratio of the cylindrical shell. It is noted that the hydrodynamic pressure can be taken as the hydrostatic pressure according to the rules of conversion in this present paper. When the hydrostatic pressure is larger than 0.8, the circular ring will be buckled at hydrodynamic pressure that can be predicted by the analytical solutions. However, when the hydrostatic pressure is smaller than 0.8, the analytical solution provides a lower limit for the predicted value especially

when the ultimate failure is taken into account. The proposed solutions can be correctly and easily used to help predict and estimate the structural performance of subsea vehicles especially when the subsea vehicles are in a very high hydrostatic pressure in the deeper parts of the ocean. The outcome of this study will help to control the velocity of the subsea vehicle considering both hydrostatic and hydrodynamic pressures in order to maintain its structural stability and prevent catastrophic failure. It will also help improve the design of vehicle geometry in terms of thickness and cross section taking into account the velocity and critical pressure from both hydrostatic and hydrodynamic pressure.

## Acknowledgments

The first author is sincerely grateful to Professor Chang-Fu Hu for his guidance. This work is financially supported by the National Natural Science Foundation of China (No. 51508238) which is in charge of the first author.

## References

Berkenpas, E.J., Henning, B.S., Shepard, C.M., Turchik, A.J., Robinson, C.J., Portner, E.J., Li, D.H., Daniel, P.C. and Gilly, W.F. (2018), "A Buoyancy-Controlled Lagrangian Camera Platform for In Situ Imaging of Marine Organisms in Midwater Scattering Layers", *IEEE J. Oceanic Eng.*, **43**(3), 595-607. https://doi.org/10.1109/JOE.2017.2736138

Cho, Y.S., Oh, D.H. and Paik, J.K. (2019), "An empirical formula for predicting the collapse strength of composite cylindrical-shell structures under external pressure loads", *Ocean Eng.*, **172**, 191-198. https://doi.org/10.1016/j.oceaneng.2018.11.028

Constable, S., Kowalczyk, P. and Bloomer, S. (2018), "Measuring marine self-potential using an autonomous underwater vehicle", *Geophys. J. Int.*, **215**(1), 49-60. https://doi.org/10.1093/gji/ggy263

Durban, D. and Libai, A. (1972), "Buckling of a Circular Cylindrical Shell in Axial Compression and SS4 Boundary Conditions", *AIAA Journal*, **10**(7), 935-936. https://doi.org/10.2514/3.50251

Enrichetti, F., Bavestrello, G., Coppari, M., Betti, F. and Bo, M. (2018), "Placogorgia coronata first documented record in Italian waters: Use of trawl bycatch to unveil vulnerable deep-sea ecosystems", *Aquatic Conser.*: *Marine Freshwater Ecosyst.*, **28**(5), 1123-1138. https://doi.org/10.1002/aqc.2930

Faridmehr, I., Jokar, M.J., Yazdanipour, M. and Kolahchi, A. (2019), "Hydraulic and structural considerations of dam's spillway-a case study of Karkheh Dam, Andimeshk, Iran", *Struct. Monitor. Maint.*, *Int. J.*, **6**(1), 1-17. https:// doi.org/10.12989/smm.2019.6.1.001

Franzoni, F., Degenhardt, R., Albus, J. and Arbelo, M.A. (2019a), "Vibration correlation technique for predicting the buckling load of imperfection-sensitive isotropic cylindrical shells: An analytical and numerical verification", *Thin-Wall. Struct.*, **140**, 236-247. https://doi.org/10.1016/j.tws.2019.03.041

Franzoni, F., Odermann, F., Wilckens, D., Skuķis, E., Kalniņš, K., Arbelo, M.A. and Degenhardt, R. (2019b), "Assessing the axial buckling load of a pressurized orthotropic cylindrical shell through vibration correlation technique", *Thin-Wall. Struct.*, **137**, 353-366. https://doi.org/10.1016/j.tws.2019.01.009

Fujita, K. and Nosaka, T. (2002), "Dynamic Buckling Behavior of an Elastic Beam Subjected to Horizontal and Vertical Excitations Simultaneously", *ASME 2002 Pressure Vessels and Piping Conference*, **46563**, 127-133. https://doi.org/10.1115/PVP2002-1407

Ganesan, N. and Pradeep, V. (2005), "Buckling and vibration of circular cylindrical shells containing hot liquid", *J. Sound Vib.*, **287**(4), 845-863. https://doi.org/10.1016/j.jsv.2004.12.001

Gomez, M., Moulton, D.E. and Vella, D. (2016), "The shallow shell approach to Pogorelov's problem and the breakdown of 'mirror buckling'", *Proceedings of the Royal Society A*: *Mathematical*, *Physical and Engineering Sciences*, **472**(2187), 20150732. https://doi.org/10.1098/rspa.2015.0732

Hernandez, E., Naranjo, C. and Vellojin, J. (2020), "Modelling of thin viscoelastic shell structures under Reissner–Mindlin kinematic assumption", *Appl. Mathe. Modell.*, **79**, 180-199. https://doi.org/10.1016/j.apm.2019.10.031

Hongwei, M., Guoqiang, C., Shanyuan, Z. and Guitong, Y. (1999), "Experimental studies on dynamic plastic buckling of circular cylindrical shells under axial impact", *Acta Mechanica Sinica*, **15**(3), 275-282. https://doi.org/10.1007/BF02486155

Hu, C.F. and Huang, Y.M. (2019), "In-plane nonlinear elastic stability of pin-ended parabolic multi-span continuous arches", *Eng. Struct.*, **190**, 435-446. https://doi.org/10.1016/j.engstruct.2019.04.013

Hu, C.F., Pi, Y.L., Gao, W. and Li, L. (2018), "In-plane non-linear elastic stability of parabolic arches with different rise-to-span ratios", *Thin-Wall. Struct.*, **129**, 74-84. https://doi.org/10.1016/j.tws.2018.03.019

Li, H., Cong, G., Li, L., Pang, F. and Lang, J. (2019a), "A semi analytical solution for free vibration analysis of combined spherical and cylindrical shells with non-uniform thickness based on Ritz method", *Thin-Wall. Struct.*, **145**, 106443. https://doi.org/10.1016/j.tws.2019.106443

Li, H., Cong, G., Li, L., Pang, F. and Lang, J. (2019b), "A semi analytical method for free vibration analysis of composite laminated cylindrical and spherical shells with complex boundary conditions", *Thin-Wall. Struct.*, **136**, 200-220. https://doi.org/10.1016/j.tws.2018.12.009

Lu, S., Wang, W., Chen, W., Ma, J., Shi, Y. and Xu, C. (2019), "Behaviors of Thin-Walled Cylindrical Shell Storage Tank under Blast Impacts", *Shock Vib.*, **2019**, 6515462. https://doi.org/10.1155/2019/6515462

Ma, X., Yan, J., Luan, Z., Zhang, X., Zheng, C.E. and Sun, D. (2016), "High-resolution topography measurement of PACMANUS and DESMOS hydrothermal fields using a ROV in Manus basin", *Sci. Bull.*, **61**(15), 1154-1156. https://doi.org/10.1007/s11434-016-1114-y

Maier, K.L., Brothers, D.S., Paull, C.K., McGann, M., Caress, D.W. and Conrad, J.E. (2017), "Records of continental slope sediment flow morphodynamic responses to gradient and active faulting from integrated AUV and ROV data, offshore Palos Verdes, southern California Borderland", *Marine Geology*, **393**, 47-66. https://doi.org/10.1016/j.margeo.2016.10.001

McClain, C.R. and Barry, J.P. (2010), "Habitat heterogeneity, disturbance, and productivity work in concert to regulate biodiversity in deep submarine canyons", *Ecology*, **91**(4), 964-976. https://doi.org/10.1890/09-0087.1

Narayana, Y.V., Gunda, J.B., Reddy, P.R. and Markandeya, R. (2013), "Non-linear buckling and post-buckling analysis of cylindrical shells subjected to axial compressive loads: a study on imperfection sensitivity", *Nonlinear Eng.*, **2**(3-4), 83-95. https://doi.org/10.1515/nleng-2013-0009

Okubo, M., Minami, H. and Morikawa, K. (2003), "Influence of shell strength on shape transformation of micron-sized, monodisperse, hollow polymer particles", *Colloid Polym. Sci.*, **281**(3), 214-219. https://doi.org/10.1007/s00396-002-0716-x

Pang, F., Li, H., Cui, J., Du, Y. and Gao, C. (2019), "Application of flügge thin shell theory to the solution of free vibration behaviors for spherical-cylindrical-spherical shell: A unified formulation", *Eur. J. Mech. - A/Solids*, **74**, 381-393. https://doi.org/10.1016/j.euromechsol.2018.12.003

Pi, Y.L. and Bradford, M.A. (2013), "In-plane stability of preloaded shallow arches against dynamic snap-through accounting for rotational end restraints", *Eng. Struct.*, **56**, 1496-1510. https://doi.org/10.1016/j.engstruct.2013.07.020

Qu, Y., Zhang, W., Peng, Z. and Meng, G. (2019), "Nonlinear structural and acoustic responses of three-dimensional elastic cylindrical shells with internal mass-spring systems", *Appl. Acoust.*, **149**, 143-155. https://doi.org/10.1016/j.apacoust.2019.01.009

Rizzetto, F., Jansen, E., Strozzi, M. and Pellicano, F. (2019), "Nonlinear dynamic stability of cylindrical shells under pulsating axial loading via Finite Element analysis using numerical time integration", *Thin-Wall. Struct.*, **143**, 106213. https://doi.org/10.1016/j.tws.2019.106213

Stuart, F.R., Goto, J.T. and Sechler, E.E. (1968), *The buckling of thin-walled circular cylinders under axial compression and bending*, National Aeronautics and Space Administration, Washington D.C., USA.

Sun, J.B., Xu, X.S. and Lim, C.W. (2012), "Dynamic buckling of cylindrical shells under axial impact in Hamiltonian system", *Int. J. Nonlinear Sci. Numer. Simul.*, **13**(1), 93-97. https://doi.org/10.1515/ijnsns-2011-0105

Tvergaard, V. (1983), "Plastic buckling of axially compressed circular cylindrical shells", *Thin-Wall. Struct.*, **1**(2), 139-163. https://doi.org/10.1016/0263-8231(83)90018-6

Timmins, I.J. and O'Young, S. (2009), "Marine communications channel modeling using the finite-difference time domain method", *IEEE Transact. Vehicular Technol.*, **58**(6), 2626-2637. https://doi.org/10.1109/TVT.2008.2010326

Wang, Y., Shao, S., Wang, S., Wu, Z., Zhang, H. and Hu, X. (2014), "Measurement error analysis of multibeam echosounder system mounted on the deep-sea autonomous underwater vehicle", *Ocean Eng.*, **91**, 111-121. https://doi.org/10.1016/j.oceaneng.2014.09.002

Werner, B. (2019), "Navy, Shipbuilders Working On Final Details Of Block V Virginia-Class Submarine Deal", USNI News. Available on: https://news.usni.org/2019/08/29/navy-shipbuilders-working-on-final-details-of-block-v-virginia-class-submarine-deal

Zou, R.D. and Foster, C.G. (1995), "Simple solution for buckling of orthotropic circular cylindrical shells", *Thin-Wall. Struct.*, **22**(3), 143-158. https://doi.org/10.1016/0263-8231(94)00026-V

Zou, D., Li, W., Liu, T. and Teng, J. (2018), "Two-dimensional water seepage monitoring in concrete structures using smart aggregates", *Struct. Monitor. Maint., Int. J.*, **5**(2), 313-323. https://doi.org/10.12989/smm.2018.5.2.313

*CC*